

of postsynaptic receptors, as a form of synaptic plasticity, to be a key element in associative memory formation.

Circuit mechanisms of memory. By using molecular tagging techniques, we estimate that about a third of lateral amygdala neurons undergo plasticity during the formation of a memory driven by a single conditioning block. Because not all synapses on a plastic neuron undergo modification, one neuron may potentially participate in many memories, which allows combinatorial storage of a large number of memories (48–50). Perturbing plasticity in a small fraction of lateral amygdala neurons appears to be sufficient to reduce memory function, which suggests little robustness or redundancy. Memory formation may require coordinated changes in synaptic strength, and perturbing a few plastic units may corrupt integrated function, much as the inability of a few violinists to change key properly can detectably offset a symphonic performance. Finding such sensitivity to small perturbation is striking given that large lesions (51) or advanced brain pathology (52) produce little disturbance of memory formation.

References and Notes

1. S. Freud, in *The Origins of Psychoanalysis*, M. Bonaparte, A. Freud, E. Kris, Eds. (Basic Books, New York, 1895), pp. 356–359.
2. D. O. Hebb, *Organization of Behavior* (Wiley, New York, 1949).
3. M. S. Rioult-Pedotti, D. Friedman, J. P. Donoghue, *Science* **290**, 533 (2000).
4. P. Andersen, *Philos. Trans. R. Soc. London B Biol. Sci.* **358**, 613 (2003).
5. G. Lynch, *Philos. Trans. R. Soc. London B Biol. Sci.* **358**, 625 (2003).
6. B. L. McNaughton, *Philos. Trans. R. Soc. London B Biol. Sci.* **358**, 629 (2003).
7. R. G. Morris, *Philos. Trans. R. Soc. London B Biol. Sci.* **358**, 643 (2003).
8. S. Tonegawa, K. Nakazawa, M. A. Wilson, *Philos. Trans. R. Soc. London B Biol. Sci.* **358**, 787 (2003).
9. J. Lisman, *Philos. Trans. R. Soc. London B Biol. Sci.* **358**, 829 (2003).
10. H. Eichenbaum, *Neuron* **44**, 109 (2004).
11. J. E. LeDoux, *Annu. Rev. Neurosci.* **23**, 155 (2000).
12. S. Maren, *Annu. Rev. Neurosci.* **24**, 897 (2001).
13. R. A. Nicoll, *Philos. Trans. R. Soc. London B Biol. Sci.* **358**, 707 (2003).
14. G. L. Collingridge, J. T. Isaac, Y. T. Wang, *Nature Rev. Neurosci.* **5**, 952 (2004).
15. R. C. Malenka, M. F. Bear, *Neuron* **44**, 5 (2004).
16. R. Malinow, *Philos. Trans. R. Soc. London B Biol. Sci.* **358**, 707 (2003).
17. M. Sheng, M. J. Kim, *Science* **298**, 776 (2002).
18. I. Song, R. L. Huganir, *Trends Neurosci.* **25**, 578 (2002).
19. D. Johnston et al., *Philos. Trans. R. Soc. London B Biol. Sci.* **358**, 667 (2003).
20. K. M. Harris, J. C. Fiala, L. Ostroff, *Philos. Trans. R. Soc. London B Biol. Sci.* **358**, 745 (2003).
21. C. Pittenger, E. R. Kandel, *Philos. Trans. R. Soc. London B Biol. Sci.* **358**, 757 (2003).
22. S. Choi, J. Klingauf, R. W. Tsien, *Philos. Trans. R. Soc. London B Biol. Sci.* **358**, 695 (2003).
23. D. Zamanillo et al., *Science* **284**, 1805 (1999).
24. Y. Hayashi et al., *Science* **287**, 2262 (2000).
25. M. Passafaro, V. Piech, M. Sheng, *Nature Neurosci.* **4**, 917 (2001).
26. C. F. Stevens, *Neuron* **20**, 1 (1998).
27. W. A. Carlezon Jr. et al., *Science* **277**, 812 (1997).
28. A. Bahi, F. Boyer, T. Kafri, J. L. Dreyer, *Eur. J. Neurosci.* **19**, 1621 (2004).
29. Z. Dong et al., *Proc. Natl. Acad. Sci. U.S.A.* **100**, 12438 (2003).
30. J. R. Goss et al., *Methods Mol. Biol.* **246**, 309 (2004).
31. V. M. Sandler et al., *J. Neurosci. Methods* **121**, 211 (2002).
32. R. L. Neve, A. I. Geller, *Adv. Neurol.* **79**, 1027 (1999).
33. S. A. Josselyn et al., *J. Neurosci.* **21**, 2404 (2001).
34. E. S. Faber, R. J. Callister, P. Sah, *J. Neurophysiol.* **85**, 714 (2001).
35. J. Boulter et al., *Science* **249**, 1033 (1990).
36. R. Malinow, R. C. Malenka, *Annu. Rev. Neurosci.* **25**, 103 (2002).
37. A. J. Watt, P. J. Sjöström, M. Hausser, S. B. Nelson, G. G. Turrigiano, *Nature Neurosci.* **7**, 518 (2004).
38. S. Shi, Y. Hayashi, J. A. Esteban, R. Malinow, *Cell* **105**, 331 (2001).
39. T. Takahashi, K. Svoboda, R. Malinow, *Science* **299**, 1585 (2003).
40. K. A. Goosens, S. Maren, *Learn. Mem.* **8**, 148 (2001).
41. C. B. Sananes, M. Davis, *Behav. Neurosci.* **106**, 72 (1992).
42. P. S. Bellgowan, F. J. Helmstetter, *Behav. Neurosci.* **110**, 727 (1996).
43. P. Andersen, S. H. Sundberg, O. Sveen, H. Wigstrom, *Nature* **266**, 736 (1977).
44. S. Maren, *Eur. J. Neurosci.* **12**, 4047 (2000).
45. M. A. Good, A. Johnson, D. Bannerman, N. Rawlins, R. Sprengel, paper presented at the Annual Meeting of the Society for Neuroscience, San Diego, 23 to 27 October 2004.
46. H. K. Lee et al., *Cell* **112**, 631 (2003).
47. J. A. Esteban et al., *Nature Neurosci.* **6**, 136 (2003).
48. D. Marr, *Philos. Trans. R. Soc. London B Biol. Sci.* **262**, 23 (1971).
49. P. Andersen, M. Trommald, *J. Neurobiol.* **26**, 396 (1995).
50. M. B. Moser, E. I. Moser, *J. Neurosci.* **18**, 7535 (1998).
51. M. B. Moser, E. I. Moser, E. Forrester, P. Andersen, R. G. Morris, *Proc. Natl. Acad. Sci. U.S.A.* **92**, 9697 (1995).
52. D. A. Snowdon, *Ann. Intern. Med.* **139**, 450 (2003).
53. This project was supported by DFG Ru 900/2-1 (S.R.), NIH (J.L., A.Z., R.M.), Mathers Charitable Foundation and Sloane Foundation (A.Z.), and Ale Davis and Maxine Harrison Foundation (R.M.). We thank G. Di Cristo for help with confocal microscopy; R. Neve for help and materials for viral expression system; N. Dawkins-Pisany for technical assistance; R. Tsien, G. Buzsaki, J. Hopfield, and Z. Mainen for comments on an earlier version of this manuscript; and M. Moita for helpful discussions.

Supporting Online Material

www.sciencemag.org/cgi/content/full/1103944/DC1
Materials and Methods
Figs. S1 and S2
Reference and Notes

8 November 2004; accepted 8 February 2005

Published online 3 March 2005;

10.1126/science.1103944

Include this information when citing this paper.

REPORTS

Spin-Charge Separation and Localization in One Dimension

O. M. Auslaender,^{1*} H. Steinberg,¹ A. Yacoby,^{1†} Y. Tserkovnyak,²
B. I. Halperin,² K. W. Baldwin,³ L. N. Pfeiffer,³ K. W. West³

We report on measurements of quantum many-body modes in ballistic wires and their dependence on Coulomb interactions, obtained by tunneling between two parallel wires in an GaAs/AlGaAs heterostructure while varying electron density. We observed two spin modes and one charge mode of the coupled wires and mapped the dispersion velocities of the modes down to a critical density, at which spontaneous localization was observed. Theoretical calculations of the charge velocity agree well with the data, although they also predict an additional charge mode that was not observed. The measured spin velocity was smaller than theoretically predicted.

Coulomb interactions have a profound effect on the behavior of electrons. The low-energy properties of interacting electronic systems are

described by elementary excitations, which interact with each other only weakly. In two- and three-dimensional disordered metals, they

are dubbed quasiparticles (1), as they bear a strong resemblance to free electrons (2), which are fermions carrying both charge and spin. However, the elementary excitations in one-dimensional (1D) metals, known as Luttinger liquids (3, 4), are utterly different. Each is collective and highly correlated and carries either spin or charge.

We determined the dispersions of the elementary excitations in one dimension by measuring the tunneling current, I_T , across an

¹Department of Condensed Matter Physics, Weizmann Institute of Science, Rehovot 76100, Israel. ²Lyman Laboratory of Physics, Harvard University, Cambridge, MA 02138, USA. ³Bell Labs, Lucent Technologies, 700 Mountain Avenue, Murray Hill, NJ 07974, USA.

*Present address: Geballe Laboratory for Advanced Materials, Stanford University, Stanford, CA 94305, USA.

†To whom correspondence should be addressed.
E-mail: amir.yacoby@weizmann.ac.il

extended junction between two long, ballistic, parallel wires in a GaAs/AlGaAs heterostructure created by cleaved edge overgrowth (CEO) (5). In this geometry, tunneling conserves both energy and momentum. Each tunneling event creates an electron-hole pair with total momentum $\hbar k = eBd \equiv \hbar q_B$ and total energy $E = |eV_{SD}|$, where $2\pi\hbar$ is Planck's constant, $-e$ is the electron charge, B is the magnetic field applied perpendicular to the plane of the wires, d is the distance between their centers, and V_{SD} is the voltage bias between them (supporting online text).

The rate of tunneling between the wires depends on the ease of adding an electron to one wire and a hole to the other, determined by the electron-hole spectral function, $A_{k,E}$. For weak interwire interactions, $A_{k,E}$ is a convolution of the individual particle spectral functions, which encode the overlap of electrons (or holes) with the many-body modes of the coupled wires. Near $V_{SD} = 0$, in the limit of temperature $T \rightarrow 0$, tunneling is appreciable only if $|q_B| = |k_{FU} \pm k_{FL}|$, allowing exchange of electrons between the Fermi points $k_{Fi} = \pi n_i/2$, where n_i is electron density in sub-band i and $i = U$ or L stands for sub-bands in the upper or lower wires. At finite energies, interactions broaden the peaks of the individual particle spectral functions, in particular giving them a distribution of momenta. In spite of this, at $E = 0$, $A_{k,E}$ is sharply peaked at $k = |k_{FU} \pm k_{FL}|$ for homogeneous wires (6). Thus, as long as momentum is conserved in the wires and in the tunnel junction, tunneling near $V_{SD} = 0$ is enhanced at the same $B \geq 0$ values as without interactions

$$B_{\pm} = \frac{\hbar}{ed} |k_{FU} \pm k_{FL}| \quad (1)$$

For inhomogeneous wires, the $V_{SD} = 0$ line shape of the spectral function encodes information on the low-energy momentum distribution of the many-body states (7).

Interactions become more important as the energy associated with them increases relative to kinetic energy. To increase this ratio, we reduced electron density in the wires by applying negative voltage, V_G , to a 2- μm top gate lying on the surface of the device. Figure 1A shows a typical low-energy measurement of $\partial I_T / \partial V_G$, as a function of V_G and B (supporting online text). The derivative was measured in order to be sensitive only to the signal from the section of the device where density was controlled by the gate. This was done by adding a small ac component to V_G . A zero-bias anomaly (5, 7) was avoided by setting $V_{SD} = 100 \mu\text{V}$. This measurement, as well as all those reported here, was performed at 0.25 K.

Figure 1B shows the typical behavior of B_{\pm} . At high values of V_G , tunneling was appreciable only in a narrow range around B_{\pm} . As a function of V_G , B_{\pm} evolved continuously, following the behavior of k_{FU} and k_{FL} , which allowed us to

invert Eq. 1 and extract the density in each sub-band (Fig. 1C) (5) (supporting online text). In practice, each wire contained several sub-bands for most of the V_G range. Tunneling was observed only between sub-bands with the same number of nodes (e.g., between sub-band 1 in the upper wire and sub-band 1 in the lower wire or between 2 in the upper wire and 2 in the lower wire). Tunneling within each pair of sub-bands, one sub-band in each wire, gave rise to a similar set of features.

The dispersions of the modes can be determined for every density in the regime where we observed the B_{\pm} peaks. The dispersions are traced by the singularities of $A_{k,E}$ at finite energy and momentum (Fig. 2, A and B). For noninteracting electrons (Fig. 2A), the curves resulting from tunneling either from or to a Fermi point produce four curves: two shifted copies of the dispersion in each of the two wires (5).

Finite interactions split the singularities of $A_{k,E}$ (Fig. 2B) because of two effects. The first is spin-charge separation, caused by intrawire interactions, which creates two

modes for each noninteracting mode. The second effect is mode mixing, caused by interwire interactions. Generally, the mixed modes are carried by both wires, giving rise to four independent velocities (supporting online text). This results in three identical copies of each of the four dispersions. At the limit of weak tunneling, the spin modes do not couple, and as a result each dispersion branch in Fig. 2A splits into a spin mode and two coupled charge modes, creating four curves near $|q_B| = |k_{FU} - k_{FL}|$ and two sets of three curves near $|q_B| = |k_{FU} + k_{FL}|$ (Fig. 2B).

The tunneling current, $I_T(V_{SD}, B)$, is proportional to $A_{k,E}$, the singularities of which are peaks for the parameters of our experiment (6). During a scan of V_{SD} and B , $I_T(V_{SD}, B)$ changes abruptly with a change in the number of modes that can be excited with the available energy and momentum, where $A_{k,E}$ is peaked. The curve along which this happens gives the dispersion of a mode, $E(k)$. In particular, the slope at $V_{SD} = 0$ gives the dispersion velocity, $v = \hbar^{-1} \partial E / \partial k$. For the experimentally relevant case of weak tunneling, we expected ten such

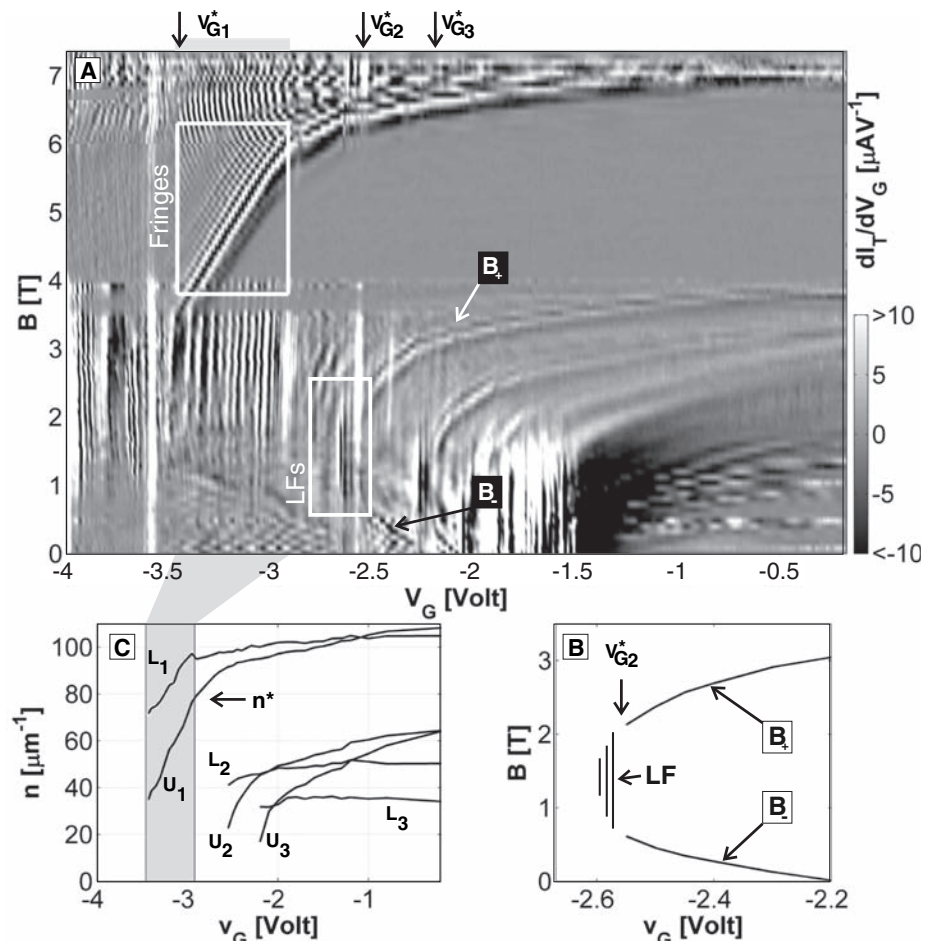
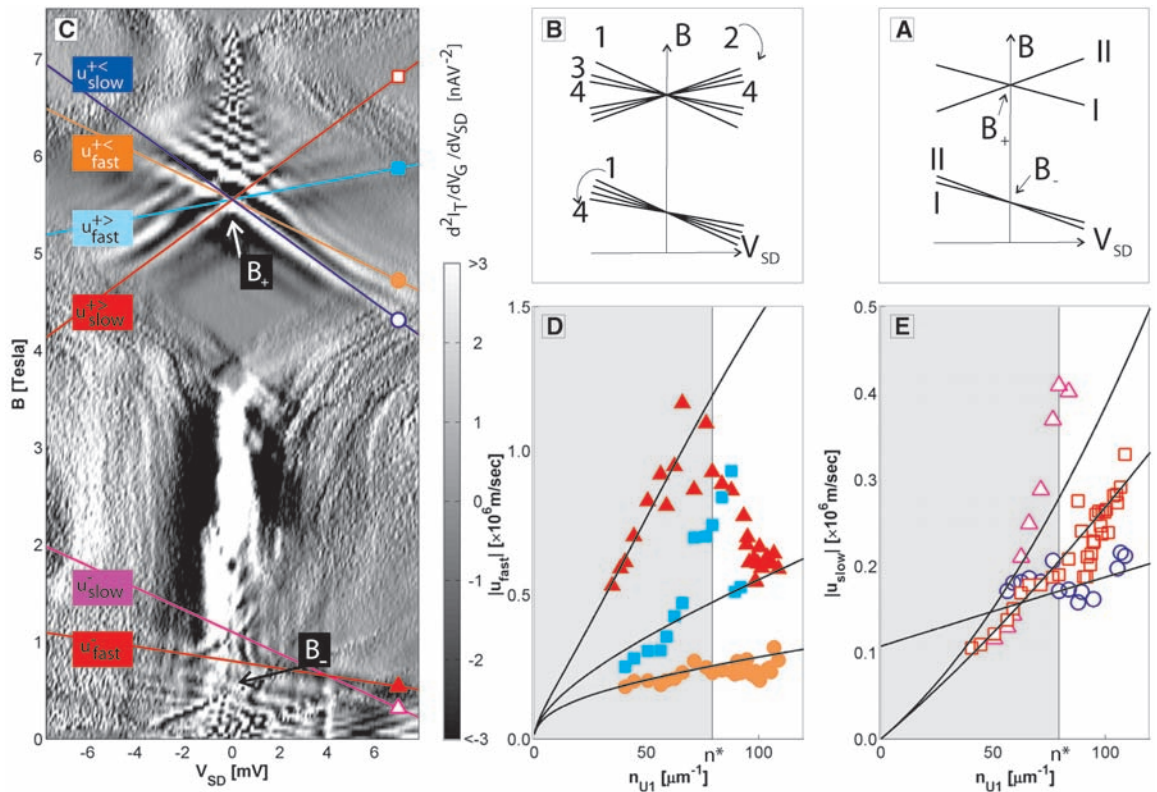


Fig. 1. (A) Gray-scale plot of $\partial I_T(V_G, B) / \partial V_G$. Onset of LFs for $V_G < V_G^*$ are marked by arrows; Fringes are finite-size fringes. (B) Zoom on the trace of B_{\pm} for sub-band 2. At V_G^* , B_{\pm} are replaced by LFs, drawn schematically. (C) Dependence of density in sub-bands 1 to 3 on V_G . U_i and L_i represent the upper- and lower-wire sub-band i . The gray box marks the regime with a single occupied sub-band in each wire ($-3.45 \text{ V} < V_G < -2.90 \text{ V}$), which starts below upper-wire density n^* .

Fig. 2. (A and B) Illustration of the position of the singularities of $A_{k,E}$ with eV_{SD} replacing E and B replacing k . (A) For noninteracting electrons, there are four curves. *I*, copies of lower wire dispersion; *II*, copies of upper wire dispersion. (B) With interactions, there are 10 curves: three duplicates of each mixed charge mode (marked 3 and 4) and two copies of each spin mode (marked 1 and 2). (C) Numerical derivative, with respect to B , of the measured $\partial I_T(V_{SD}, B)/\partial V_G$ at $V_G = -3.00$ V. Finite-size fringes appear for $B > B_+$ and $B < B_-$. All extracted slopes are marked and offset for clarity. Triangles represent slopes extracted near B_- , giving $|u_{fast}^-|$ (filled) $>$ $|u_{slow}^-|$ (empty); squares represent positive slopes near B_+ , giving $|u_{fast}^+|$ (filled) $>$ $|u_{slow}^+|$ (empty); circles represent negative slopes near B_+ , giving $|u_{fast}^+|$ (filled) $>$ $|u_{slow}^+|$ (empty). (D and E) Apparent velocities, u , versus density, n_{U1} . Each wire has a single occupied sub-band in the shaded region. (D) Dependence of u values calculated for small slopes on density. Overlaid curves



were calculated by setting v in Eq. 2 to v_{c-} from Eq. 4 and solving for u^\pm . (E) Dependence of u values calculated for large slopes on density. Overlaid curves were calculated by setting $v_{sU,L} = v_{FU,L}/1.25$ in Eq. 2.

intercepts (Fig. 2B) but only four different magnitudes of slope.

To determine the dependence of the dispersions on density, we measured $\partial I_T(V_{SD}, B)/\partial V_G$ for different values of V_G , ranging from 0 V to -3.45 V. A typical result from the regime where each wire had a single sub-band, $-3.45 < V_G < -2.9$ V, is shown in Fig. 2C. The peaks that appeared in Fig. 1A at B_\pm split and move with a slope that gives an apparent velocity $u = d^{-1}(\partial B/\partial V_{SD})_{V_G}^{-1} = 0$. Accompanying these peaks are finite-size fringes (8).

Six slopes appear in Fig. 2C, two near B_- and four near B_+ . Both B_- slopes are negative, giving $|u_{slow}^-| < |u_{fast}^-|$. Near B_+ , there are two negative slopes, giving $|u_{slow}^+| < |u_{fast}^+|$, and two positive slopes, giving $|u_{slow}^+| < |u_{fast}^+|$. For each scan, we extracted all discernable slopes. The results are summarized in Fig. 2, D and E, where they are plotted versus the density of electrons in the first sub-band of the upper wire, n_{U1} . In the shaded area, which extends up to $n^* \approx 80 \mu\text{m}^{-1}$, as extracted from Fig. 1A, only one sub-band is occupied per wire.

The unexpected presence of six different branches of u in Fig. 2, D and E, wrongly suggests that the coupled wires have more than four independent modes. The error lies in assuming that the band-filling induced by a finite V_{SD} is negligible (9). In reality, V_{SD} induces charge transfer between the wires,

which is controlled by the mutual capacitance, endowing k_{FU} and k_{FL} with a V_{SD} dependence. Thus, the actual excitation velocity is given by

$$v = \frac{|u^\pm|}{1 \pm \gamma_\pm u^\pm} \quad (2)$$

where \pm refers to the crossing point, B_\pm , near which u^\pm is extracted. The value of γ_\pm depends on the capacitance matrix of the wires and was calculated with a simple model (supporting online text). The model consisted of two wires of radius r , separated from each other by a distance $d \gg r$ and from a nearby gate by a distance $D_G/2 \gg d$. Because we applied V_{SD} to the upper wire, keeping the lower wire grounded, the energetic cost of adding charge to the wires is given to quadratic order in excess electron density, δn_i , by $\sum_i (E_{Fi} \delta n_i + e^2 c_{i1}^{-1} \delta n_i^2) + \frac{1}{2} \sum_{i,j} e^2 \delta n_i c_{ij}^{-1} \delta n_j - e \delta n_U V_{SD}$, where i, j run over wire indices U and L; $E_{Fi} = \hbar^2 k_{Fi}^2 / (2m)$ is the Fermi energy, $c_{i1}^{-1} = \pi \hbar / (2e^2 v_{Fi})$; m is the band mass of electrons; $v_{Fi} = \hbar k_{Fi} / m$ is the Fermi velocity in wire i ; and c_{ij}^{-1} are elements of the inverse capacitance matrix. In the random phase approximation (1), the first term in this expression is kinetic energy, and the second is Coulomb interaction energy. By assumption, the inverse capacitance of each wire to the gate (c_{UU}^{-1} and c_{LL}^{-1}) is identical: $c_G^{-1} = (2\pi\epsilon)^{-1} \log[D_G/r]$. The inverse capacitance

between the wires $c_{UL}^{-1} = c_{LU}^{-1}$ is $c_M^{-1} = (4\pi\epsilon)^{-1} \log[1 + (D_G/d)^2]$. Here $r = 10$ nm and $d = 30$ nm. $D_G = 70$ nm is the distance of the wires to a parallel layer of dopants. Using $D_G = 500$ nm, the distance to the top gate, has only minor influence because of the log. The dimensions are roughly the molecular beam epitaxy growth parameters of the heterostructure and were not adjusted. The result of applying Eq. 2 is presented in Fig. 3. Clearly, the model is successful when each wire has only one occupied sub-band: All three fast branches collapse on a single curve for $n_{U1} < n^*$, and all slow branches collapse on two curves (supporting online text).

The same model for interactions that corrects for band-filling allows identifying the branches in Fig. 3. For this, we turn to the Hamiltonian of the coupled wires, which consists of a free electron part and an interacting part. Taking a long length approximation and bosonizing (10), we get

$$H = \sum_{i=1}^N \sum_{s=\uparrow, \downarrow} \int_0^\infty dx \left[\frac{p_{is}^2(x)}{2mn_{is}} + \frac{m}{2} n_{is} v_{Fis}^2 q_{is}^2(x) \right] + \sum_{i,j=1}^N \frac{e^2 c_{ij}^{-1}}{2} \sum_{s,s'=\uparrow, \downarrow} n_{is} n_{js'} \int_0^\infty dx q_{is}^s(x) q_{js'}^{s'}(x) \quad (3)$$

The sums run over all N occupied sub-bands and over both spin orientations. The density

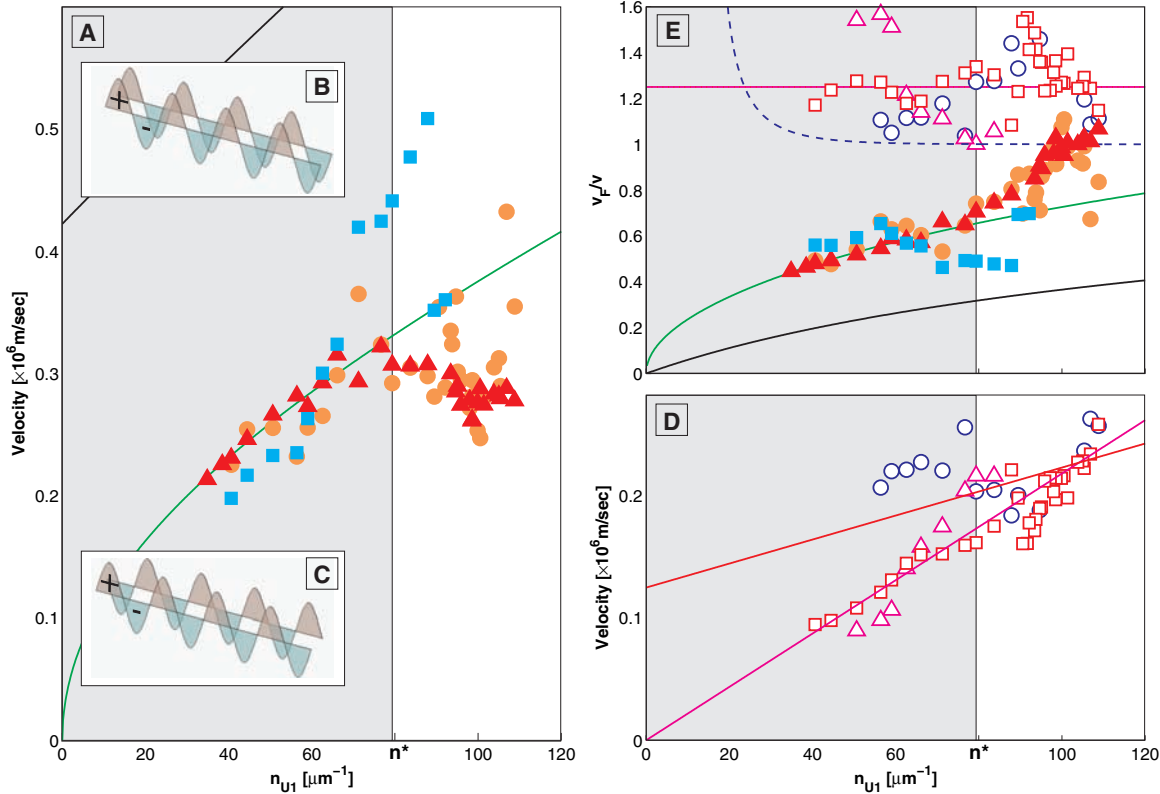


Fig. 3. Excitation velocity versus density. (A) Velocities obtained from Fig. 2D. Curves are the charge velocities v_{c-} (green) and v_{c+} (black) (Eq. 4). (B and C) Illustration of the symmetric/antisymmetric coupled-wire mode (+, excess positive charge, -, excess negative charge). (D) Velocities obtained from Fig. 2E. The lines are $v_{sU} = v_{FU}/1.25$ (magenta) and $v_{sL} = v_{FL}/1.25$ (red). The scale is the same as in (A). (E) Plot of v_F/v for the velocities in (A) and (D). v_F was calculated from n_{U1} in all cases except for $v_F/v_{sL}^{+<}$ and v_F/v_{sL}^{-} . In the latter two cases, v_F was calculated from the density in the first sub-band in the lower wire. The red and magenta curves from (D) overlap here.

of spin orientation s in sub-band i is $n_{is} = n_i/2$, q'_{is} is the gradient of the displacement operator, and p_{is} is the conjugate momentum.

Within this model, which neglects back-scattering, the velocities of the coupled-wire modes are found by diagonalizing Eq. 3 with a canonical transformation. This yields spin velocities equal to the Fermi velocities. For a single mode in each wire, $N = 2$, the two charge velocities are (10)

$$v_{ct}^2 = \frac{v_{cU}^2 + v_{cL}^2}{2} \pm \left[\left(\frac{v_{cU}^2 - v_{cL}^2}{2} \right)^2 + v_{FU}v_{FL} \left(\frac{2e^2}{\pi\hbar} c_M^{-1} \right)^2 \right]^{1/2} \quad (4)$$

Here v_{ci} is the charge velocity in each individual wire (11): $v_{ci}/v_{Fi} = \sqrt{1 + U_i/(2E_{Fi})}$, where $U_i = e^2 n_i / c_G$ is the interaction energy. Physically \pm corresponds to symmetric or antisymmetric excitations (Fig. 3, B and C). When the wires are identical, both modes are carried equally by both wires, but when the densities differ, as in the experiment, the symmetric mode is carried primarily by the more occupied wire, the lower wire, whereas the antisymmetric mode is carried primarily by the upper wire.

We have overlaid the result of Eq. 4 on the corrected velocities in Fig. 3, A and E. The fast velocities follow the calculated v_{c-} closely for $n_{U1} < n^*$, attesting to the validity of the model and leading us to associate them with the antisymmetric charge mode. The faster v_{c+} , on the other hand, is com-

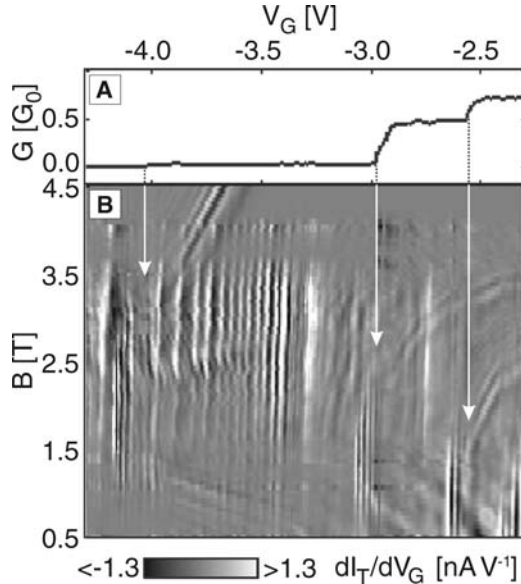


Fig. 4. (A) Two-terminal conductance of the upper wire as a function of V_G , measured by applying a dc voltage bias of 100 μ V along the wire. The step height deviates from the universal $2e^2/h$ because of the indirect upper wire contact (27, 28). This measurement depends very weakly on B , which is 1.3 T here. (B) Simultaneous measurement $\partial I_T(V_G, B)/\partial V_G$, showing that localization is concurrent with the conductance drops.

pletely absent from the data. This is to be expected near B_- , where tunneling creates interacting electron-hole pairs that propagate together, excitations that are almost completely antisymmetric. On the other hand, near B_+ none of the excitation branches should be suppressed, as they are all excited by tunneling, leaving the issue of the complete absence of the symmetric mode unresolved.

Turning to the slow branches in Fig. 3, D and E, we find linear dependence on the

bare Fermi velocities, $v_{si} = v_{Fi}/f_i$, where $f_U = f_L = 1.25$. The linearity and the fact that $f_i > 1$, suggest that these modes are the spin modes. Theoretically, one expects a spin velocity equal to v_F as long as back-scattering is weak, whereas stronger back-scattering reduces it below v_F (12–17). For example, one group (14, 15), using Monte Carlo simulations, found that the expression $f_{\text{pert}} = 1/\sqrt{1 - V_{2kf}/(\pi\hbar v_F)}$ (supporting online text) gives an upper bound to the ratio between the v_F and v_S . However, a plot of f_{pert}

in Fig. 3E shows that f_{pert} does not account for the deviation of f_i from unity.

Further examination of Fig. 1A down to the depletion of each sub-band in the upper wire reveals that the continuous evolution of each set of B_{\pm} peaks is replaced by a series of vertical streaks, dubbed localization features (LFs). These occur in a small range of V_G below $V_{\text{Gi}}^* = -3.45, -2.55, \text{ and } -2.20 \text{ V}$, for each of the three upper-wire sub-bands we observed. Each set of LFs signals an abrupt change in the momentum-space content of the wave function in the depleting sub-band.

Above V_{Gi}^* , finite-size fringes for $B < B_-$ and $B > B_+$ accompany the B_{\pm} peaks, signifying that the states in both wires contain only wave numbers higher than the Fermi wave number and implying that they are extended (8). The location of the fringes at $B < B_-$ and $B > B_+$ indicates that the potential along the nonuniform upper wire has a hump, with a typical length given by the period $h/(e\Delta B_{\text{fringe}}d) \approx 0.75 \mu\text{m}$, consistent with the barrier the surface gate induces.

Below V_{Gi}^* , we find that each LF fills a broad range in B , lying roughly between the extrapolations of B_{\pm} . This implies that the wave function of the state along the upper wire is localized. We are thus led to conclude that the B streaks signify a qualitative change in the self-consistent potential at V_{Gi}^* , which marks a transition between an extended state and a localized state. The localized states appear while the more occupied sub-bands are still fully conducting, in contrast to a recent study of inhomogeneous wires (18).

The localization transition affects transport along the upper wire. Figure 4A shows the two-terminal conductance along this wire, $G(V_G, B)$, which is quantized. The stepwise decrease of $G(V_G, B)$ with density is a hallmark of ballistic transport in a wire (19). We were able to measure $G(V_G, B)$ simultaneously with $\partial I_T(V_G, B)/\partial V_G$, by recording both the dc current along the upper wire and the ac component of the tunneling current (supporting online text). The positions of the steps in $G(V_G, B)$, which have a very weak dependence on B , are concurrent with the localization transitions apparent in Fig. 4B. We thus conclude that electrons in a sub-band cease to conduct because of localization while their density is still finite.

The localization transition hints that bound states come into existence over the barrier induced by the top gate, which we used to vary the density. The possibility of this occurring has been addressed in the context of the 0.7-anomaly in point contacts (20–23). Using a variety of theoretical tools, it was found that, when the density is low enough, a bound state may exist over the barrier (16, 24–26). Our measurements show clear evidence for this scenario in long 1D channels. Finally, 0.7-anomaly-like features

are observed regularly in the conductance steps of CEO wires similar to ours (23). Further work is needed to show a direct link between the 0.7-anomaly and the observed localization features.

References and Notes

1. P. Nozières, D. Pines, *The Theory of Quantum Liquids* (Perseus, Cambridge, MA, 1999), ed 3.
2. B. L. Altshuler, A. G. Aronov, *Electron-Electron Interaction in Disordered Systems*, A. L. Efros, M. Pollak, eds. (North-Holland, Amsterdam, 1985), pp. 1–153.
3. S.-I. Tomonaga, *Prog. Theor. Phys.* **5**, 544 (1950).
4. J. M. Luttinger, *J. Math. Phys.* **4**, 1154 (1963).
5. O. M. Auslaender et al., *Science* **295**, 825 (2002).
6. D. Carpentier, C. Peça, L. Balents, *Phys. Rev. B* **66**, 153304 (2002).
7. Y. Tserkovnyak, B. I. Halperin, O. M. Auslaender, A. Yacoby, *Phys. Rev. B* **68**, 125312 (2003).
8. Y. Tserkovnyak, B. I. Halperin, O. M. Auslaender, A. Yacoby, *Phys. Rev. Lett.* **89**, 136805 (2002).
9. D. Boese, M. Governale, A. Rosch, U. Zülicke, *Phys. Rev. B* **64**, 085315 (2001).
10. K. A. Matveev, L. I. Glazman, *Phys. Rev. Lett.* **70**, 990 (1993).
11. C. L. Kane, M. P. A. Fisher, *Phys. Rev. B* **46**, 15233 (1992).
12. C. F. Coll, *Phys. Rev. B* **9**, 2150 (1974).
13. H. J. Schulz, *Phys. Rev. Lett.* **71**, 1864 (1993).
14. C. E. Creffield, W. Häusler, A. H. MacDonald, *Europhys. Lett.* **53**, 221 (2001).
15. W. Häusler, L. Kecke, A. H. MacDonald, *Phys. Rev. B* **65**, 085104 (2002).
16. K. A. Matveev, *Phys. Rev. Lett.* **92**, 106801 (2004).
17. V. V. Cheianov, M. B. Zvonarev, *Phys. Rev. Lett.* **92**, 176401 (2004).

18. K. J. Thomas et al., *J. Phys. Condens. Matter* **16**, L279 (2004).
19. C. W. J. Beenakker, H. van Houten, in *Solid State Physics*, H. Ehrenreich, D. Turnbull, eds. (Academic Press, San Diego, CA, 1991), vol. 44, pp. 1–228.
20. K. J. Thomas et al., *Phys. Rev. Lett.* **77**, 135 (1996).
21. S. M. Cronenwett et al., *Phys. Rev. Lett.* **88**, 226805 (2002).
22. D. J. Reilly et al., *Phys. Rev. Lett.* **89**, 246801 (2002).
23. R. de Picciotto, L. N. Pfeiffer, K. W. Baldwin, K. W. West, *Phys. Rev. Lett.* **92**, 036805 (2004).
24. Y. Meir, K. Hirose, N. S. Wingreen, *Phys. Rev. Lett.* **89**, 196802 (2002).
25. K. Hirose, Y. Meir, N. S. Wingreen, *Phys. Rev. Lett.* **90**, 026804 (2003).
26. O. P. Sushkov, *Phys. Rev. B* **67**, 195318 (2003).
27. A. Yacoby et al., *Phys. Rev. Lett.* **77**, 4612 (1996).
28. R. de Picciotto, H. L. Stormer, L. N. Pfeiffer, K. W. Baldwin, K. W. West, *Nature* **411**, 51 (2001).
29. We thank G. Fiete, Y. Oreg, and J. Qian for discussions. Supported in part by the U.S.-Israel Binational Science Foundation, European Commission Research Training Network contract no. HPRN-CT-2000-00125, and NSF grant no. DMR 02-33773. Y.T. is supported by the Harvard Society of Fellows.

Supporting Online Material

www.sciencemag.org/cgi/content/full/308/5718/88/DC1
SOM Text

Fig. S1

References and Notes

23 November 2004; accepted 22 February 2005
10.1126/science.1107821

Simultaneous Tomography and Diffraction Analysis of Creep Damage

A. Pyzalla,^{1*} B. Camin,² T. Buslaps,³ M. Di Michiel,³ H. Kaminski,¹
A. Kottar,¹ A. Pernack,² W. Reimers²

Creep damage by void nucleation and growth limits the lifetime of components subjected to loading at high temperatures. We report a combined tomography and diffraction experiment using high-energy synchrotron radiation that permitted us to follow in situ void growth and microstructure development in bulk samples. The results reveal that void growth versus time follows an exponential growth law. The formation of large void volumes coincides with texture evolution and dislocation density, reaching a steady state. Creep damage during a large proportion of sample creep life is homogeneous before damage localization occurs, which leads to rapid failure. The in situ determination of void evolution in bulk samples should allow for the assessment of creep damage in metallic materials and subsequently for lifetime predictions about samples and components that are subject to high-temperature loading.

The efficiency of electricity-generating plants and gas turbines depends strongly on their components' sustainability of loading at high

temperatures. The service lifetime of these components in most cases is controlled by creep-induced cavity growth. In order to quantify the remnant lifetime of creep-loaded components, models have been proposed that have their basis in parameters characterizing microstructure damage (1–4). Microscopic methods have been used to determine, for example, the fraction of grain boundaries damaged by cavities. Creep damage has thus only been determined from two-dimensional images. Because microscopy also necessitates

¹Technische Universität (TU) Wien, Institute of Material Science and Technology, Karlsplatz 13-308, A-1040 Wien, Austria. ²TU Berlin, Institute of Material Science and Technology, Sekr. BH18, Ernst-Reuter-Platz 1, D-10587 Berlin, Germany. ³European Synchrotron Radiation Facility (ESRF), BP220, F-38043 Grenoble, France.

*To whom correspondence should be addressed.
E-mail: anke.pyzalla@tuwien.ac.at